Journal of Alloys and Compounds 509 (2011) 8433–8440

Contents lists available at ScienceDirect

Journal of Alloys and Compounds

journal homepage: www.elsevier.com/locate/jallcom

Structural, optical and charge transport study of rutile TiO_2 nanocrystals at two calcination temperatures

Archana Maurya [a,*], Pratima Chauhan [a], Sheo K. Mishra [b], Rajneesh K. Srivastava [b]

[a] UGC Centre of Advanced Studies, Department of Physics, University of Allahabad, Allahabad 211002, India
[b] Department of Electronics and Communication, University of Allahabad, Allahabad 211002, India

ARTICLE INFO

Article history:
Received 17 January 2011
Received in revised form 26 May 2011
Accepted 30 May 2011
Available online 6 June 2011

Keywords:
Rutile TiO_2 nanocrystals
X-ray diffraction
Photoconductivity (PC)

ABSTRACT

In this study the influence of two different calcination temperatures 80 °C and 450 °C on the structural, optical and charge transport properties of rutile TiO_2 nanocrystals has been investigated. TiO_2 nanocrystals have been prepared at low temperature by a simple hydrolysis method using titanium tetrachloride as starting precursor. The results of X-ray diffraction (XRD) showed that the prepared nanocrystals have a rutile tetragonal crystalline structure. Specific surface area of 80 °C and 450 °C calcinated rutile TiO_2 nanocrystals are 25.38×10^5 cm^2/g and 7.61×10^5 cm^2/g respectively, which has been calculated by X-ray diffraction data. Williamson–Hall plot results indicate the presence of compressive strain at 80 °C and tensile strain at 450 °C. Ultraviolet–visible (UV–vis) absorption spectroscopy is used to calculate the band gap of the material and the shift in absorption edge and it has been observed that the absorption spectra are strongly modified by the calcination temperature. The red-shift in photoluminescence (PL) is attributed to the change in strain from compressive to tensile. Photoconductivity (PC) measurements showed that capture cross-section of 80 °C (R1) and 450 °C (R2) calcinated rutile nanocrystals are 55.10×10^{-10} and 39.50×10^{-10} cm^2 respectively. High value of electron life-time, low value of radiative recombination and a four order increase in photogenerated charge carriers have been reported for the rutile TiO_2 nanocrystals calcinated at 450 °C.

1. Introduction

Exploring innovative mesostructured materials have greatly inspired research interest since the first discovery of the silicate M41S family in 1992 [1]. Among these novel materials to be pursued non-silica mesoporous materials have attracted remarkable attention [2–5]. TiO_2 is one of the most investigated materials among non-silica mesoporous materials owing to its many applications in the field of photocatalysis, gas and humidity sensors, water treatment, self-cleaning, solar cells, photo electrochemical cells, protective coatings on optical elements and bio-analytical chemistry [6–10]. Because of its brightness and very high refractive index it is also widely employed as a pigment to provide whiteness and opacity to products such as paints, coatings, plastics, papers, inks, sunscreen, foods, medicines as well as most toothpastes [11–17]. It is a wide-band gap semiconductor with relatively strong ionicity, being advantageous in photoassisted dissociation of molecules. TiO_2 shows a diverse heterogeneity of crystalline phases, whereby it is possible to find it in anatase, rutile or brookite form [18]. In its pure form it is an *n*-type semiconductor with indirect band gaps of 3.2 eV for anatase and 3.02 eV for rutile between the full oxygen 2p valence band and titanium 3d states at the bottom of the conduction band. Compared to anatase, rutile TiO_2 is chemically more stable because anatase converts to rutile when heated [19–22]. Also, rutile TiO_2 possesses a superior light scattering property [23,24] which is beneficial from the perspective of effective light harvesting.

The transport of charge carriers in nanocrystalline semiconductors that are being used in the new generation photovoltaic devices is of fundamental importance. The nature of charge transport depends primely on the structure, morphology, the effect of defects at grain boundaries and the extremely large surface area of the nanomaterials [25]. Different types of native defects such as various traps and foreign imperfections can cause considerable change in the electrical and optical properties of semiconductor since they give rise to charge center acting as donors and acceptors [26]. Despite the fact that during the last decade a large number of reports have appeared on the electron transport through nanostructured anatase TiO_2 [27–31], the nature of charge transport is still under debate for pure rutile TiO_2 due to complexity of mechanism [32].

Various methods [33–37] have been reported in literature to synthesize nanocrystalline TiO_2. In this paper we have approached a simple hydrolysis method to prepare pure rutile TiO_2

---

* Corresponding author. Tel.: +91 05322460993.
E-mail addresses: v.arch17@gmail.com (A. Maurya), mangu167@yahoo.co.in (P. Chauhan).

0925-8388/$ – see front matter. Crown Copyright © 2011 Published by Elsevier B.V. All rights reserved.
doi:10.1016/j.jallcom.2011.05.108

nanocrystals. The prepared sample after calcination at two different temperatures has been employed to understand the structural, optical and charge transport properties of rutile TiO_2. Also, an attention has been drawn to understand the dynamics of the induced photogenerated charge carriers with the filling and emptying the trap centers, recombination rate, life-time and capture cross-section. We have shown that different types of native defects and surface morphology such as effective surface area greatly affect the electrical and optical properties of the semiconductor.

2. Experimental

2.1. Sample preparation

For preparing the sample we have used anhydrous titanium (IV) chloride (Merck), ethanol (Merck) and double distilled deionized water. 2 mL of titanium (IV) chloride ($TiCl_4$) was dissolved in 10 mL of absolute ethanol under constant magnetic stirring. Then 50 mL double distilled deionized water was also added dropwise in above solution with constant stirring. The entire process was carried out in an ice bath at 0 °C. A white color solution appeared which was stirred for another 3 h and then aged in static condition at 0 °C for four days. The resulting precipitate was recovered by centrifugation process followed by washing several times with double distilled water to remove the dissolved HCl. The sample was then calcinated at temperatures 80 °C and 450 °C. In order to get finally divided TiO_2 nanopowder the samples were grinded in mortar and pestle. We have named R1 for 80 °C calcinated sample and R2 for 450 °C calcinated sample.

2.2. Experimental characterization techniques

Rigaku D-max XRD with fixed Cu-Kα line (λ = 1.5416 Å) was used for recording X-ray diffraction spectra operating at 30 kV and 30 mA at steps 0.05° in the 2θ range 20–60°. Transmission electron microscopy (TEM) and high resolution transmission electron microscopy (HRTEM) were performed by using Tecnai 30 G2 S-Twin electron microscope operating at 300 kV accelerating voltage. The band gaps of the samples were investigated by optical absorption studies carried out using a UV–visible spectrophotometer (Lambda 35 Perkin Elmer in the range 200–800 nm). Photoluminescence (PL) spectra of the prepared samples were measured at room temperature using LS 55 Perkin Elmer spectrophotometer with 375 nm excitation line of Xenon discharge lamp, equivalent to 20 kV for 8 μs duration with pulse width at half height <10 μs. The photoconductivity (PC) of TiO_2 nanocrystals has been measured using thick film of powder without any binder. For PC measurements, a cell was formed by putting a thick layer of powdered samples in between two Cu electrodes etched on a Cu plate (PCB), having a spacing of 1 mm. The powdered layer was pressed with transparent glass plate. This glass plate has a slit for providing illumination area of 0.25 cm^2. In this cell type device, the direction of illumination is normal to field across the electrodes. The cell was mounted in a dark chamber with a slit where from the light is allowed to fall over the cell. The photo-response was measured in air using 300 W mercury lamp of 365 nm light intensity as a photo-excitation source. A stabilized dc field (50–500 V/cm) was applied across the cell to which a dc nanoammeter, NM-122 (Scientific Equipment, Roorkee) for the measurement of current and RISH Multi 15S with adapter RISH Multi SI-232 were connected in series. Before measuring PC of the sample, the cell is first kept in dark till it attains equilibrium.

3. Results and discussion

3.1. Structural study

X-ray diffraction pattern gives information about crystalline structure, grain size and lattice strain. Fig. 1 shows the X-ray diffraction spectra of samples R1 and R2. All the diffraction peaks in both the samples are assigned well to tetragonal rutile crystalline phase of TiO_2 with a reference pattern (lattice: primitive, space group $P4_2$/mnm [136], lattice constant $a = b = 4.594$ Å and $c = 2.958$ Å, JCPDS file No. 860147). No impurity peaks have been observed in addition to TiO_2 which indicates high purity of the sample. As observed from the recorded XRD spectra, the peak intensity of all the reflections increases several times with increasing calcination temperature and crystalline phase becomes more pronounced, where the lattice plane (1 1 0) is most predominant. An earlier report of Charles Kittel has revealed that the X-ray intensities can be represented well by the free atom value [38]. Thus the increase in X-ray intensity can be attributed to the availability of appropriate number of free electrons at such high temperature.

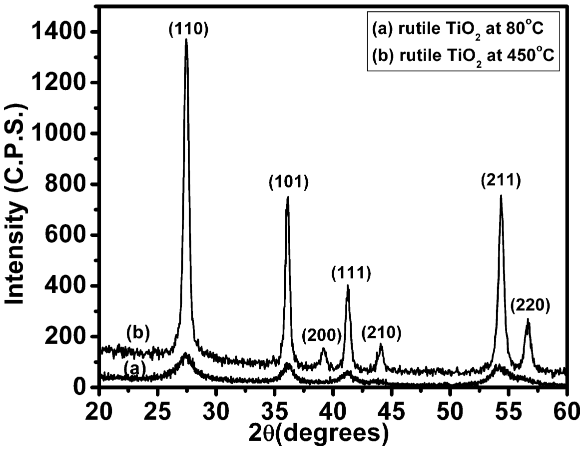

Fig. 1. X-ray diffraction patterns of pure rutile TiO_2 nanoparticles prepared via simple hydrolysis method and calcinated at 80 °C (R1) and 450 °C (R2).

The crystalline size (D) of the samples R1 and R2 were calculated using Debye-Scherrer formula i.e. $D = 0.9\lambda/\beta\cos\theta$, where λ is the wavelength of the X-rays, β is the full width at the half maximum intensity (FWHM) and θ is the Bragg diffraction angle [39]. Corresponding to the maximum intensity peak, crystallite size for sample R1 was calculated to be 5.6 nm which is close to the standard value of Bohr exciton radius of TiO_2 (~5.0 nm). The crystallite size for sample R2 was calculated to be 18.2 nm.

Williamson–Hall plot provide information about lattice strain and effective particle size, i.e. particle size with zero strain, present in the sample. Using Williamson–Hall plot, we have calculated the lattice strain and effective particle size through the following relation [40]:

$$\frac{\beta \cos \theta}{\lambda} = \frac{1}{\varepsilon} + \frac{\eta \sin \theta}{\lambda} \tag{1}$$

where β, ε and η are the full width at half maximum (FWHM) in radians, the effective particle size and the effective strain, respectively. Fig. 2(a) and (b) shows the Williamson–Hall plot, i.e. the plot between $\beta\cos\theta/\lambda$ versus $\sin\theta/\lambda$ for the samples R1 and R2, respectively. It has been reported in literature that a negative slope in the plot indicate the presence of compressive strain [41,42], whereas the appearance of positive slope indicate the possibility of tensile strain [43]. We have observed a negative slope for sample R1 which reveals the presence of compressive strain and a positive slope for sample R2 revealing the presence of tensile strain in rutile TiO_2. From the slope of the graph the compressive strain for sample R1 was calculated to be 0.59% whereas the tensile strain for sample R2 comes out to be 0.79%. The intercept on the $\beta\cos\theta/\lambda$ axis give the effective particle size corresponding to zero strain. The effective particle size for samples R1 and R2 comes out as 11.29 nm and 15.94 nm respectively.

In case of tetragonal crystal structure ($a = b \neq c$), the lattice constant is calculated using the following formula:

$$\frac{1}{d_{h\,k\,l}^2} = \frac{h^2 + k^2}{a^2} + \frac{l^2}{c^2} \tag{2}$$

where $d_{h\,k\,l}$ is the interplaner separation corresponding to Miller indices h, k, l, and 'a', 'c' are the lattice constants. For the samples R1 and R2 the calculated structural parameters corresponding to strongest peak (1 1 0) are given in Table 1. When compared to bulk rutile TiO_2 ($a = b = 4.594$ Å and $c = 2.958$ Å), an increase in the value of lattice constants 'a' (='b') and a decrease in lattice constant 'c' for sample R1 have been observed. This can be owed due to the compressive lattice strain, which was calculated using the values $(\Delta a/a) = 0.62\%$ and $(\Delta c/c) = 0.57\%$, as they result from

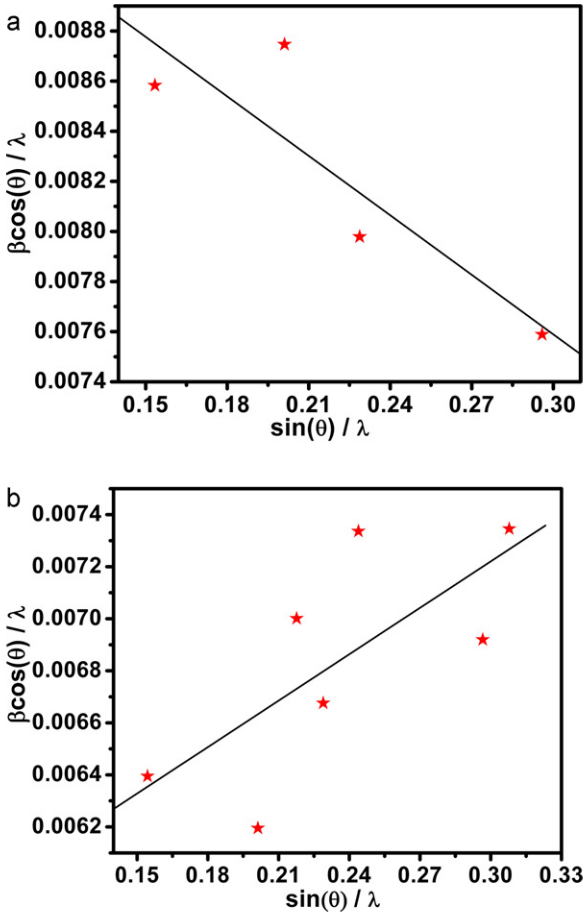

Fig. 2. Williamson–Hall plots of TiO_2 nanopowder (a) calcinated at 80 °C and (b) calcinated at 450 °C for the size and strain analysis.

Table 1. However, for sample R2 a decrease in lattice constants $a(=b)$ as well as in c have been noticed which indicates the development of internal tensile strain. Jiang et al. have previously reported that decrease in size is an important cause for the lattice contraction among the particles [44]. It is well known that crystallinity increases whereas FWHM value decreases with increase in temperature and vice versa. An estimation of FWHM implies a much more perfect order of crystallinity of sample R2 (Table 1). From Table 1 it can also be seen that for sample R2, d-spacing and the volume of unit cell decreases, a result which has been reported previously [45]. A reduction in these values signifies the closeness of lattice plane and an increase of density of the layers.

Further structural characterization of the rutile TiO_2 samples was carried out using TEM image analysis. Fig. 3(a) and (b) shows the TEM images of sample R1 and R2 respectively. These TEM images reveal the formation of aggregated spherical TiO_2 nanocrystallites of size 3–5 nm for sample R1 and 12–15 nm for sample R2. The HRTEM images of samples R1 and R2 are shown in Fig. 4(a) and (b) respectively. It can be seen that the lattice fringes of sample R2 is more clear and sharp than sample R1 which also indicates high crystalline nature of sample R2. The lattice fringes shown in the HRTEM image of Fig. 4(a) corresponds to distances $d_{0.33}$ Å of (1 1 0) plane reflection in addition to $d_{0.22}$ Å of (1 1 1) plane reflection of rutile TiO_2. However, Fig. 4(b) shows (1 1 0) plane reflections combined with the presence of (1 1 1) and (1 0 1) ($d_{0.25}$ Å) plane reflections. It is clear from HRTEM images of both the samples that the preferential orientation of rutile TiO_2 occurs along the (1 1 0) plane.

Table 1
Structural parameters of rutile TiO_2 as a function of calcination temperatures corresponding to strongest peak (1 1 0).

Calculated parameters	Rutile TiO_2 Annealing temperature	
	80 °C	450 °C
FWHM	1.43261 ± 0.01642	0.41896 ± 0.00487
Grain size (nm)	5.6	18.2
Lattice constants	$a = b = 4.6224$ Å $c = 2.9410$ Å	$a = b = 4.5898$ Å $c = 2.9058$ Å
d-Spacing	3.2572 Å	3.2442 Å
Unit cell volume, a^2c (Å^3)	62.8391	61.2144
Density, ρ (g/cm^3)	4.2218	4.3338
Specific surface area, S_a (cm^2/g)	25.38×10^5	7.61×10^5

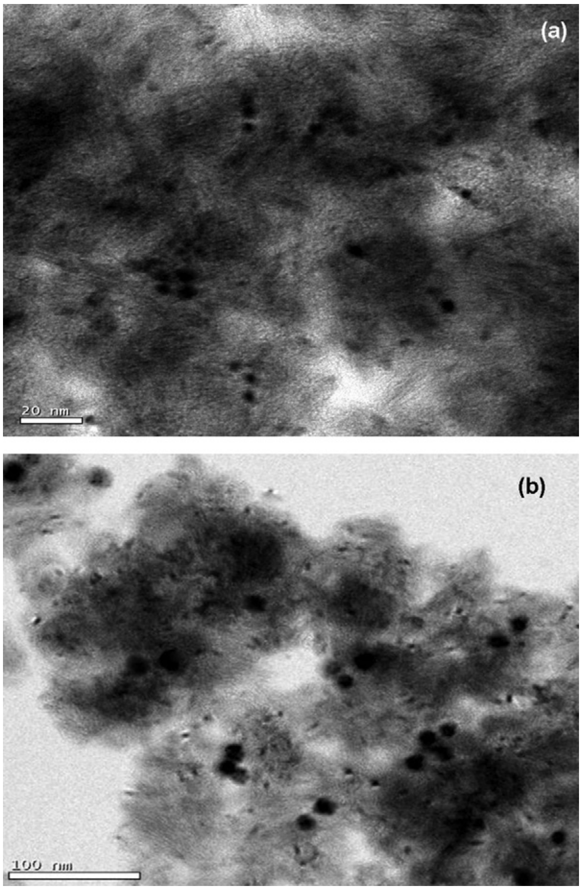

Fig. 3. TEM images of rutile TiO_2 for two different calcination temperatures (a) calcinated at 80 °C (R1) and (b) calcinated at 450 °C (R2).

We have calculated the X-ray density for both the samples by the formula:

$$\rho = \frac{nM}{NV} \tag{3}$$

where n is the number of atoms per unit cell, M is the molecular weight, N is Avogadro's constant and V is the volume of the unit cell. Jagriti Pal et al. have calculated the X-ray density for the Co_3O_4 nanocrystal [46]. Here we have done the same calculation for the tetragonal rutile TiO_2 nanocrystal. Since, rutile TiO_2 (tetragonal, $P4_2/mnm$) has two formula units per unit cell [47], the formula for X-ray density takes the form:

$$\rho = \frac{2M}{NV} \tag{4}$$

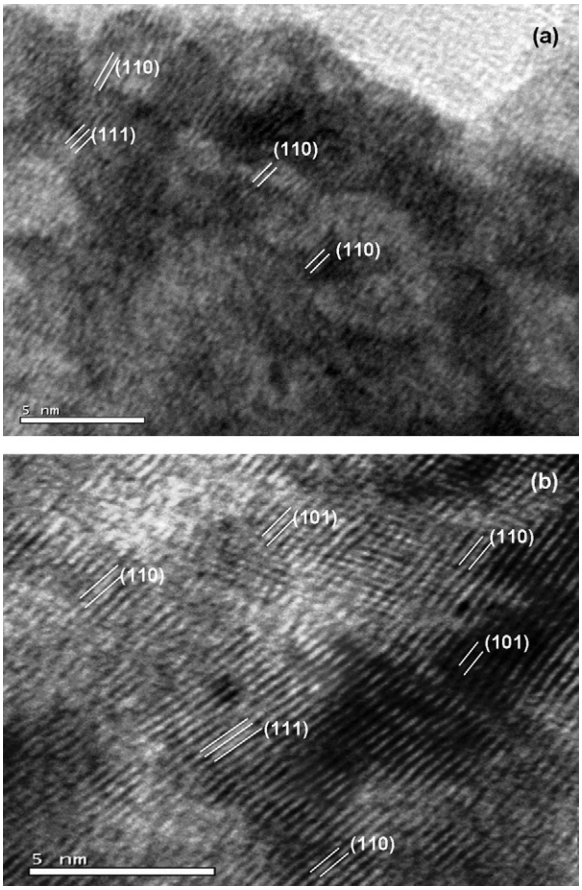

Fig. 4. HRTEM images of rutile TiO_2 (a) calcinated at 80 °C (R1) and (b) calcinated at 450 °C (R2).

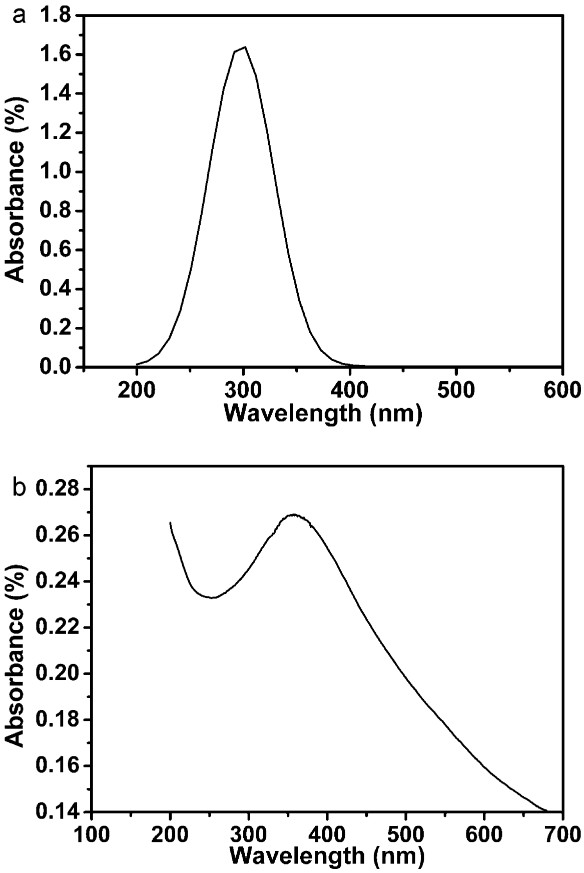

Fig. 5. UV–visible absorption spectra of as synthesized rutile TiO_2 (a) calcinated at 80 °C (R1) and (b) calcinated at 450 °C (R2).

Further, the specific surface area of the rutile TiO_2 nanocrystals along the strongest peak (1 1 0) is calculated using the formula:

$$S_a = \frac{6}{D \times \rho} \tag{5}$$

where D and ρ are the crystallite size and X-ray density of the rutile TiO_2 nanocrystals respectively. For samples R1 and R2 the calculated values of X-ray density, ρ and specific surface area S_a are given in Table 1. These results also indicate that the density of rutile TiO_2 nanocrystals increases with the increase in calcinations temperature. However, the surface area decreases approximately three times in magnitude. It should be noted that the total surface energy increases with the overall surface area. An increased surface area attributes high value of surface energy and hence a higher number of active surface sites.

3.2. Optical absorbance study

Fig. 5(a) and (b) shows the results from optical absorption measurements for the samples R1 and R2, respectively. The optical absorption spectra of sample R2 shows a shift in the absorption edge towards longer wavelength in comparison to R1, which was likely caused by increase in particle size, crystallinity and decrease in charge difference between Ti and O atoms. The variation of density and the structural modifications may be responsible for changes in the shape of the fundamental absorption edge observed in the two samples [45].

The optical band gap energy of the corresponding samples is calculated by Tauc plot. The absorption band gap energy can be determined by the following equation [48]:

$$(\alpha h\upsilon)^n = B(h\nu - E_g) \tag{6}$$

where $h\nu$ is the photon energy, α is the absorption coefficient, B is a constant relative to the material and n is a value that depends on the nature of transition (2 for a direct allowed transition, 2/3 for direct forbidden transition, and 1/2 for indirect allowed transition). The $(\alpha h\nu)^{1/2}$ versus $h\nu$ extrapolated to $\alpha = 0$ gives the absorption band gap energy. The band gap energy evaluated for sample R1 (Fig. 6(a)) is 3.16 eV which is larger than the value of 3.02 eV for bulk rutile TiO_2. This can be explained with quantum size effect (QSE). For most semiconductors an increase in energy gap with decreasing particle size leads to a blue shift of the optical absorption edge [49]. The curve in Fig. 6(b) can be extrapolated to give band gap energy of 1.14 eV. It can be seen that the optical band gap of sample R2 decreases upon calcination which was likely caused by the increase in crystallization of the sample [50]. Also, reduction in the band gap for sample R2 can be attributed to charge transfer from bulk to the surface of the nanocrystal and this could be very supporting for the photocurrent generation upon photoexcitation.

3.3. Photoluminescence study

Fig. 7 illustrates the photoluminescence features of samples R1 and R2. Since excitation was carried out at equal excitation wavelength of 375 nm, the differences in emission intensities must originate from the differences in surface properties at two calcinations temperatures. We notice that the emission band shifts towards higher wavelength for sample R2. This shift can be

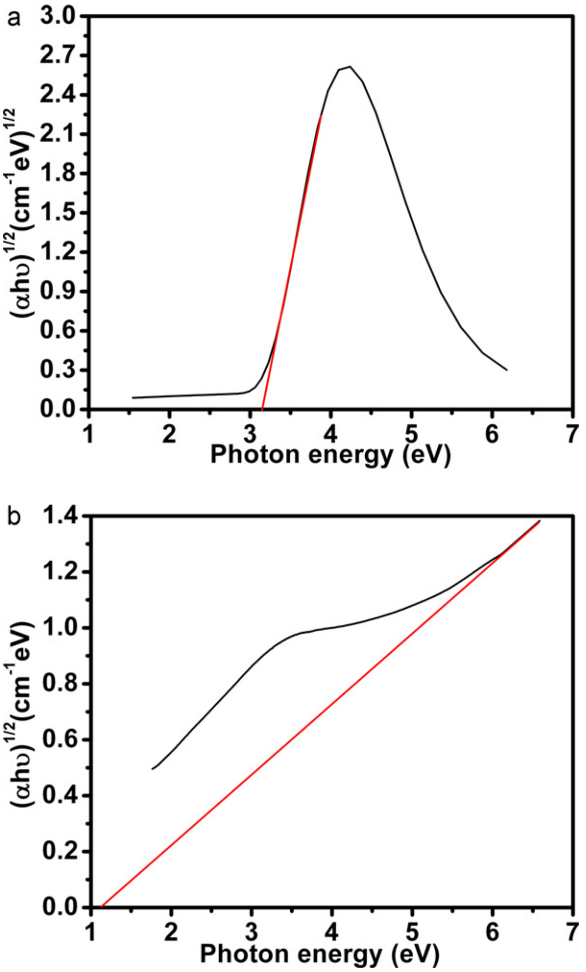

Fig. 6. Tauc plots of $(\alpha h\nu)^{1/2}$ as a function of photon energy (a) calcinated at 80 °C (R1) and (b) calcinated at 450 °C (R2).

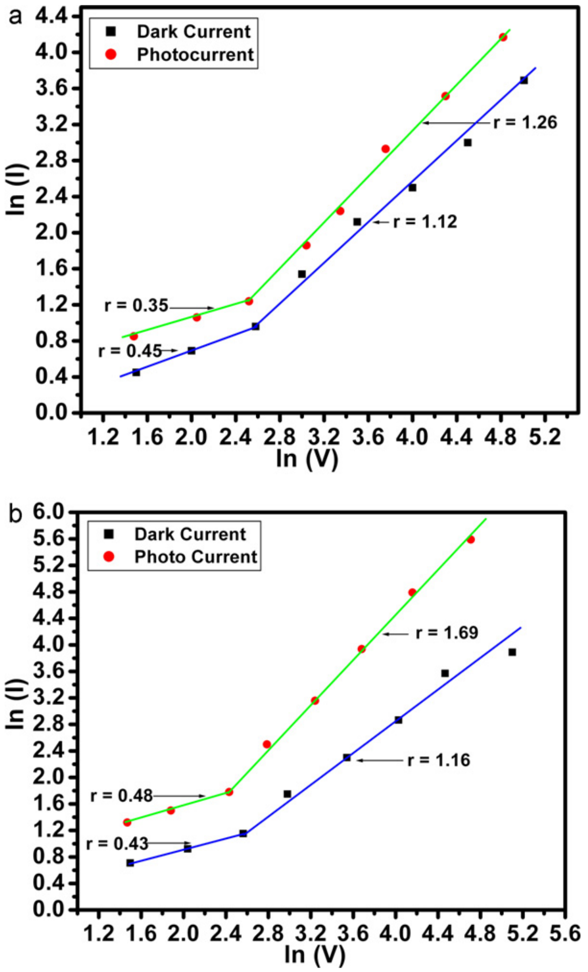

Fig. 8. Variation of photocurrent and dark current as a function of applied voltage for rutile TiO_2 nanocrystals (a) calcinated at 80 °C (R1) and (b) calcinated at 450 °C (R2).

attributed to change in lattice strain from compressive to tensile. Aumer et al. have reported that a change in strain from compressive to tensile results in a red-shift in PL [51]. In Fig. 7(a), the broad high-energy PL band at ~2.9 eV for sample R1 corresponds to the lowest indirect transition $\Gamma_{1b} \rightarrow X_{1a}$ [52]. However, the PL band at ~2.4 eV for sample R2 revealed the presence of shallow trap level induced due to the presence of oxygen vacancies [53]. The observed quenching in PL intensity for sample R2 can be owed due to the growth role of the nonradiative recombination centers [54], the presence of tensile strain induced to the crystallization and a reduction in surface dangling bonds which would enhance band gap emission.

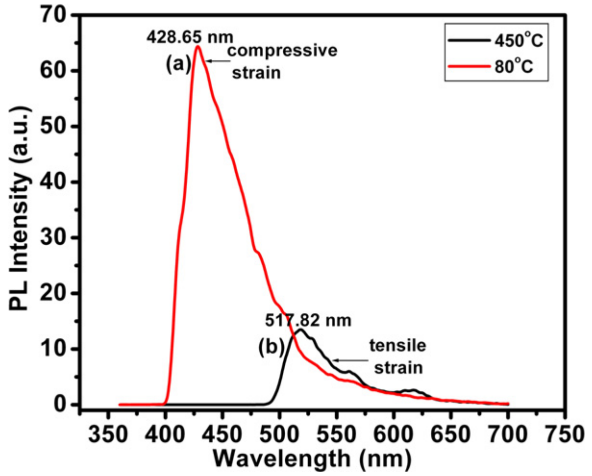

Fig. 7. Photoluminescence spectrum of rutile TiO_2 nanocrystal (a) calcinated at 80 °C (R1) and (b) calcinated at 450 °C (R2) at excitation wavelength of 375 nm.

3.4. Charge transport study

3.4.1. Effect of field

Fig. 8(a) and (b) shows the variation of dark current I_{DC} and photogenerated current I_{PC} ($I_{PC} = I_{Total} - I_{DC}$) with applied voltage on ln–ln scale for sample R1 and R2, respectively. The ln(I) versus ln(V) curves follows the power law, $I_p \propto V^r$, where r represents the slope at the low and high voltages regime. For both samples, dark current I_{DC} and photocurrent I_{PC} vary sublinearly ($r < 1$) and superlinearly ($r > 1$) at the low and the high voltages regime, respectively. This sub-linear to super-linear variation is attributed to flow of trap limited as well as space charge limited current inside the material [55–57]. The current at higher voltages arise from a space charge of excess carriers injected from one of the electrodes. This mechanism is known as space charge limited current. Also, if the material has traps, the dark current will be determined by traps and trap-limited, space charge-limited current [56].

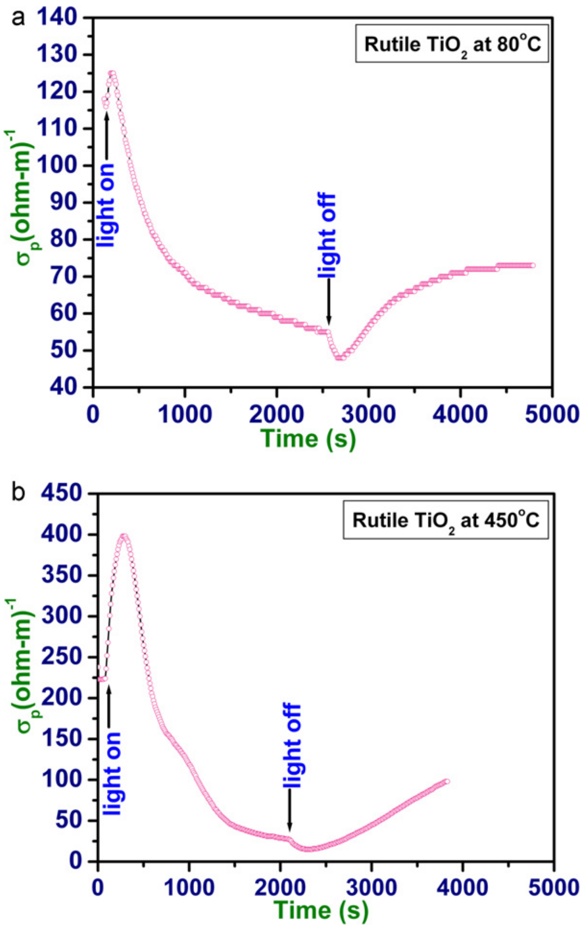

Fig. 9. Photoconductivity of rutile TiO_2 nanoparticles (a) calcinated at 80 °C (R1) and (b) calcinated at 450 °C (R2), illuminated at light intensity of 365 nm as a function of time as the light was switched on and off. The direction of illumination is normal to the field across the electrodes.

3.4.2. Rise and decay time response photoconductivity measurements

Now, to characterize the charge transport properties related to that of electron traps in the rutile TiO_2 nanocrystals in more detail, we have performed time-resolved photoconductance measurements. Fig. 9(a) and (b) shows the photoconductance transients for samples R1 and R2, obtained on optical excitation at $\lambda = 365$ nm. Since the photon energy used is well above the bandgap of rutile TiO_2, optical excitation leads to the formation of electron hole pairs. We found that PC for sample R1 increases slowly and then suddenly decreases under illumination time. After the illumination is switched off PC decreases and then gradually again increases slowly. The sudden relaxation of PC under the illumination time can be attributed to the carrier detrapping effects and fast recombination of electrons and holes at the grain boundaries in the nanocrystal. The processes of photogeneration, band-to-band recombination, electron trapping and electron scavenging are illustrated in Fig. 10. Rather slow increase in dark conductivity in both types of samples after the illumination is switched off can probably be related to the intensity of applied field to the samples. When the field applied to the samples is sufficiently high, a pulse of light will trigger the powder which results an increase in dark conductivity even after the light is switched off [58]. In addition from Fig. 9(a) and (b), we have also observed the appearance of negative photoconductivity. Borshchevskii [59] suggested that the effect was due to flaws and impurities in the crystals. More precisely, Stockmann [60] suggested that if minority carriers are optically freed from centers, a negative photoconductivity will result because of the rapid recombination of these minority carriers with majority carriers. As can be seen from Fig. 9(a) and (b), the negative photoconductivity get reduced in case of sample R2 revealing that sample R2 is structurally more perfect and much more free from flaws and impurities.

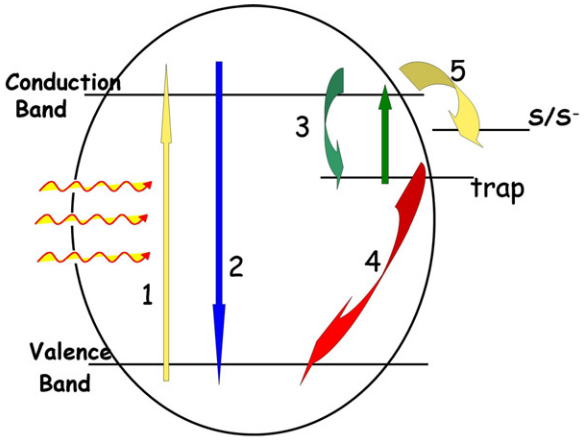

Fig. 10. Diagram representing various processes occurring in photoconductivity (1) photogeneration, (2) band-to-band recombination, (3) electron trapping, (4) hole trapping and (5) electron scavenging. S/S$^-$ represents the electron scavenging state on the surface of the nanoparticles.

On the basis of multi-trapping model (MT), an enormous increase of the PC for sample R2 could be expected due to the thermal activation of trapped electrons by reducing the native defects. In our case, PC in the rutile TiO_2 nanocrystals is found to be almost temperature-dependent. A four order rise in PC in case of sample R2 can be explained by following Boltzmann statistics. According to Boltzmann statistics a temperature rise would result in an increase of four orders of magnitude in the ratio of the number of conduction band electrons and trapped electrons and hence four orders rise in PC could be expected. The change in PC exhibited by samples R1 and R2 as a function of time is shown in Fig. 11. Both the samples of rutile TiO_2 shows a significant increase of the change in PC. The highest change in PC occurs for sample R2, 7.45×10^{-3}. Sample R1 possesses only a change in PC of the order of 1.94×10^{-3}. This drop in PC is possibly due to the trapping of the electrons by the surface native defects where the photogeneration rate is found to be responsible for the rise in photocurrent [61]. A large change in PC is indicative of the high concentration of photogenerated electrons and holes.

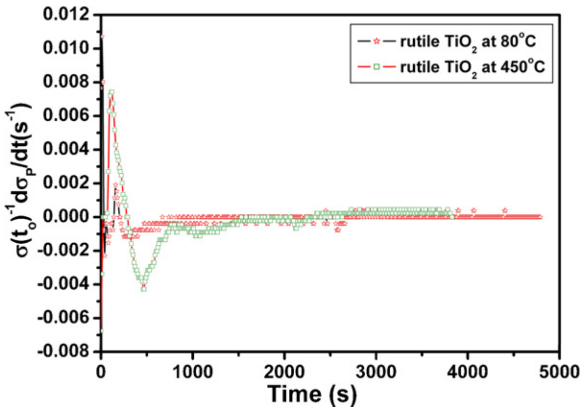

Fig. 11. Change percent in photoconductivity of rutile TiO_2 nanoparticles calcinated at 80 °C (R1) and 450 °C (R2) as a function of time (t).

Table 2
The rise and decay time constants τ_r (s), τ_d (s), probability of an electron escaping (p) from the trap, trap ionization energies (trap depth, eV) of trap corresponding to exponentials, mobility of electrons, rate of radiative recombination, carrier life-time and capture cross-section.

Calculated parameters	Rutile TiO_2 Annealing temperature	
	80 °C	450 °C
Rise time, τ_r (s)	78.00	162.00
Decay time, τ_d (s)	63.18	136.32
$p \times 10^{-4}$	23.18	102.00
Trap depth (eV)	0.65	0.69
Mobility, μ ($cm^2\,V^{-1}\,s^{-1}$)	0.82	2.50
R ($cm^{-3}\,s^{-1}$)	3.73×10^{12}	0.61×10^{12}
Life-time (s)	0.13×10^7	0.81×10^7
Capture cross-section (cm^2)	55.10×10^{-10}	39.50×10^{-10}

3.4.3. Trap depth determination

Trap depth is defined as the energy required to remove an atom from the trap. Trap depths can be calculated from decay curves. The decay of photocurrent can be expressed as:

$$I_t = I_0 \quad \exp\frac{-t}{\tau} \tag{7}$$

where I_0 is the steady current for time-resolved decay, τ is time constant and t is the time. The trap depths can also be calculated by using the following simple decay law:

$$I_t = I_0\ \exp(-pt) \tag{8}$$

where p (=$1/\tau$) is the probability of escape of an electron from the trap per second and is given by [62]:

$$p = S \quad \exp\left(\frac{-E}{kT}\right) \tag{9}$$

where E is the trap depth for electrons below the bottom of the conduction band or top of the valance band, k is Boltzmann constant (1.381×10^{-23} J/K), T is absolute temperature in K and S is attempt to escape frequency, defined as the number per second that the quanta from the lattice vibrations (phonons) attempt to eject the electron from the trap multiplied by the probability of transition of the ejected electron to the conduction band, and is of the order of 10^9 at room temperature.

From the two relations (8) and (9), the expression for trap depth is given by:

$$E = kT\left[\ln S - \ln\left\{\ln\frac{(I_0/I_t)}{t}\right\}\right] \tag{10}$$

From time-resolved rise and decay of PC spectra, the trap depths are calculated by peeling off the decay portion of the curves into the possible number of exponentials and governed by exponential law of the current amplitude as given by Eq. (7) [63].

The rise and decay time constants τ_r (s) and τ_d (s), probability of an electron escaping from the trap and trap ionization energies (trap depth, eV) of traps corresponding to exponentials for the rutile TiO_2 nanocrystal systems are calculated and listed in Table 2. We observed that the rise and decay time constants increase approximately twice in magnitude for sample R2 compared to sample R1. This increase in rise as well as decay time constants may be associated to the decrease in the surface area which results a change in the surface adsorbed oxygen molecules. The similar phenomena has been reported by Nabanita Pal et al. and Bera et al. for the case of RB entrapped mesoporous TiO_2 [64]. For sample R1 the lower PC and its corresponding shorter rise and decay time actually reflects the faster electron–hole recombination rate. The calculated probability of escaping of an electron from the traps for sample R1 and R2 comes out to be 23.18×10^{-4} and 102.00×10^{-4}, respectively. We can relate the saturation in PC to that of trap filling and probability of escaping of electrons from these traps. The more traps are filled, the easier for an electron to escape from these traps and the quicker the saturation in PC can be achieved. For TiO_2 nanocrystals average trap-depths between 0.10 and 0.27 eV have been proposed in literature [65,66]. In our case trap depth or trap ionization energies for samples R1 comes out as 0.65 eV and for sample R2 as 0.69 eV, which is much greater than the reported value of trap depth for pure TiO_2. Gupta et al. have reported, for the case of ZnO that with the increase in impurity concentration the trap depth value decreases [67]. Also, Marin Cernea et al. have shown that calcination of TiO_2 to higher temperature causes an increase in trap depth value [24]. In our case, an increased trap depth value in comparison to reported value attributes that the prepared TiO_2 nanocrystals are largely free from impurity and defects levels and structurally more perfect.

3.4.4. Electron mobility, rate of radiative recombination, life-time and capture cross-section measurements for rutile TiO_2

By assuming the concentration of free electrons in nanocrystalline rutile $TiO_2 \approx 10^{19}\,cm^{-3}$ [68,69], we have estimated the electron mobility, the rate of radiative recombination, life-time of photoexcited carriers and capture cross-section for both the samples of rutile TiO_2 via two simple assumptions: (1) the conductivity is dominated by one type of charge carrier so that the contribution due to other can be effectively neglected and (2) the crystal stays neutral during PC process without a build up of appreciable space charge in the crystal. Since TiO_2 is an n-type semiconductor the electrical properties in it is predominantly governed by electrons. By following these assumptions the electron mobility has been calculated by the expression:

$$\sigma = ne\mu \tag{11}$$

where σ is the PC of the sample in $\Omega^{-1}\,cm^{-1}$, e is the electronic charge (=1.6×10^{-19} C) and μ is the electron mobility in $cm^2\,V^{-1}\,s^{-1}$. The rate of radiative recombination per unit volume at thermal equilibrium can be expressed as [70]:

$$R = 1.78 \times 10^{22} \int_o^{\infty} n^3 K \frac{u^3}{e^u - 1} du \tag{12}$$

where n is the index of refraction (2.609 for rutile), $u = h\nu/kT$ and $K = \alpha\lambda/4\pi n$ with α absorption coefficient for the sample. The associated life-time is given by the expression:

$$\frac{1}{\tau} = R\left(\frac{1}{n} + \frac{1}{p}\right) \tag{13}$$

For an intrinsic material,

$$\tau_i = \frac{n_i}{2R} \tag{14}$$

Further, the capture cross-section has been calculated by the expression [71]:

$$S = \frac{1}{\upsilon N \tau} \tag{15}$$

where υ is the thermal velocity of the carrier = $\sqrt{}$ (2 kT/m), S is the capture cross-section of the recombination center for n-type of charge carrier and N is the density of recombination center (=radiative recombination per unit volume per unit time at thermal equilibrium). The estimated values of these parameters are given in Table 2. For sample R2 the electron mobility increases approximately three times which is due to the subsequent increase in the number of photogenerated charge carriers with the reduced density of trap states probably associated with small surface area. Kangkan et al. have reported that the increase in PC occurs due to two contributors viz. one from the resultant increase in the photogenerated charge carriers and other due to the increase in the effective mobility which is a function of temperature [72]. A high value of electron mobility for sample R2 also implies that the sample R2 is pure and structurally more perfect than sample R1. Robert Janes et al. have reported that the rate of trap related recombination increases linearly with surface area [73]. In our calculation of specific surface area and recombination rate, we have observed the same phenomena. Study on electron life-time, rate of radiative recombination and capture cross-section attributes high value of life-time and low value of radiative recombination and capture cross-section for sample R2 which resembles the results of Harish et al. for the case of Sn/ZnO thin film based photodetector [74]. They have also reported a weakening of capture cross-section with the subsequent increase of electron life-time.

4. Conclusions

In this paper the effect of temperature on structural, optical and charge transport properties of rutile TiO_2 has been investigated. We observed that crystallinity and density of rutile TiO_2 nanocrystals increases whereas surface area decreases with increasing calcination temperature. The band gap energy evaluated for sample R1 is 3.36 eV which is larger than the value of 3.02 eV for bulk rutile TiO_2. Sample R2 shows band gap of 1.14 eV, which was likely caused by the increase in crystallization of the sample. Williamson–Hall plot reveals the presence of compressive strain at 80 °C and a tensile strain at 450 °C calcination temperature. This change in strain is also responsible for the observed variation in PL peak position and peak intensity. In our case trap depth occurs at much greater value than the previously reported value of trap depth for TiO_2. A four order rise in PC in case of sample R2 can be explained by following Boltzmann statistics. Calculated values of electron life-time, rate of radiative recombination and capture cross-section attributes high value of life time and low value of radiative recombination and capture cross-section for sample R2 compared to sample R1.

Acknowledgements

The authors wish to thank Prof. A.C. Pandey, Nanotechnology Application Center, University of Allahabad, Allahabad, India for providing XRD and PL facilities. We are thankful to Prof. Ram Gopal, Dept of Physics, University of Allahabad, Allahabad, India for providing the UV–visible absorption facility. One of the authors Ms. Archana would like to acknowledge UGC for granting research fellowship.

References

[1] C.T. Kresge, M.E. Leonowicz, W.J. Roth, J.C. Vartuli, J.S. Beck, Nature 359 (1992) 710–712.

[2] G.J.A.A. Soler-Illia, C. Sanchez, B. Lebeau, J. Patarin, Chem. Rev. 102 (2002) 4093–4138.

[3] Y.-Y. Lyu, S.H. Yi, J.K. Shon, S. Chang, L.S. Pu, S.-Y. Lee, et al., J. Am. Chem. Soc. 126 (2004) 2310–2311.

[4] Z.-R. Tian, W. Tong, J.-Y. Wang, N.-G. Duan, V.V. Krishnan, S.L. Suib, Science 276 (1997) 926–930.

[5] P. Yang, D. Zhao, D.I. Margolese, B.F. Chmelka, G.D. Stucky, Chem. Mater. 11 (1999) 2813–2826.

[6] S.U.M. Khan, M. Al-Shahry, W.B. Ingler Jr., Science 297 (2002) 2243–2245.

[7] K. Hou, B.Z. Tian, F.Y. Li, Z.Q. Bian, D.Y. Zhao, C.H. Huang, J. Mater. Chem. 15 (2005) 2414–2420.

[8] L. Songqin, C. Aicheng, Langmuir 21 (2005) 8409–8413.

[9] E. Topoglidis, E.G. Cass Anthony, G. Gilardi, S. Sadeghi, N. Beaumont, J.R. Durrant, Anal. Chem. 70 (1998) 5111–5113.

[10] K.J. McKenzie, F. Marken, Langmuir 19 (2003) 4327–4331.

[11] L. Caballero, K.A. Whitehead, N.S. Allen, J. Verran, Dyes Pigments 86 (2010) 56–62.

[12] J. Labille, J. Feng, C. Botta, D. Borschneck, M. Sammut, M. Cabie, et al., Environ. Pollut. 158 (2010) 3482–3489.

[13] X. Zhu, J. Wang, X. Zhang, Y. Chang, Y. Chen, Chemosphere 79 (2010) 928–933.

[14] X. Zhu, Y. Chang, Y. Chen, Chemosphere 78 (2010) 209–215.

[15] D.M. Gonçalves, S. Chiasson, D. Girard, Toxicol. Vitro 24 (2010) 1002–1008.

[16] R.-R. Zhu, W.-R. Wang, X.-Y. Sun, H. Liu, S.-L. Wang, Toxicol. Vitro 24 (2010) 1639–1647.

[17] I. Demetrescu, C. Pirvu, V. Mitran, Bioelectrochemistry 79 (2010) 122–129.

[18] H.L. Hu, T. Yoko, H. Kozuka, S. Sakka, Thin Solid Films 219 (1992) 18–23.

[19] J.F. Banfield, D.R. Veblen, D.J. Smith, Am. Mineral. 76 (1991) 343–353.

[20] C.T. Dervos, E. Thirios, J. Novacovich, P. Vassiliou, P. Skafidas, Mater. Lett. 58 (2004) 1502–1507.

[21] G. Madras, B.J. McCoy, A. Navrotsky, J. Am. Ceram. Soc. 90 (2007) 250–255.

[22] D.H. Lindsley, Experimental studies of oxide minerals, in: D.H. Lindsley (Ed.), Oxide Minerals: Petrologic and Magnetic Significance, Rev. Mineral., 25, 1991, pp. 69–106.

[23] J.-C. Auger, B. Stout, R.G. Barrera, F. Curiel, J. Quant. Spectrosc. Radiative Transfer 70 (2001) 675–695.

[24] M. Cernea, M. Secu, C.E. Secu, M. Baibarac, B.S. Vasile, J. Nanopart. Res. 13 (2011) 77–85.

[25] B.O. Aduda, P. Ravirajan, K.L. Choy, J. Nelson, Int. J. Photoenergy 06 (2004) 141–147.

[26] A. Serpi, J. Phys. D: Appl. Phys. 9 (1976) 1881.

[27] A. Wahl, J. Augustynski, J. Phys. Chem. B 102 (1998) 7820–7828.

[28] A. Adel, Z. Marketa, R. Jiri, Z. Arnost, K. Ladislav, J. Solid State Electrochem. 9 (3) (2005) 134–145.

[29] A. Staniszewski, S. Ardo, Y. Sun, F.N. Castellano, G.J. Meyer, J. Am. Chem. Soc. 130 (35) (2008) 11586–11587.

[30] J. Jacimovic, C. Vaju, R. Gaal, A. Magrez, H. Berger, L. Forró, Materials 3 (2010) 1509–1514.

[31] L. Cavigli, F. Bogani, A. Vinattieri, L. Cortese, M. Colocci, V. Faso, G. Baldi, Solid State Sciences 12 (2010) 1877–1880.

[32] N. Golego, S.A. Studenikin, M. Cocivera, J. Mater. Res. 14 (1999) 698–707.

[33] M. Formenti, F. Juillet, P. Meriaudeau, S.J. Teichner, P. Vergnon, J. Colloid Interface Sci. 39 (1972) 79–89.

[34] L.Y. Shi, C.Z. Li, D.Y. Fang, Mater. Rev. (Ch) 12 (1998) p23.

[35] L. Shi, C. Li, A. Chen, Y. Zhu, D. Fang, Mater. Chem. Phys. 66 (2000) 51–57.

[36] K.S. Mazdiyasni, Ceram. Int. 8 (1982) 42.

[37] M. Yan, W. Rhodes, L. Sprintger, Am. Ceram. Soc. Bull. 61 (1982) 911.

[38] C. Kittel, Introduction to Solid State Physics, seventh ed., John Wiley and Sons, Inc., Singapore, New York, 1996.

[39] B.E. Warren, X-ray Diffraction, Dover, New York, 1990, p 251.

[40] G.K. Williamson, W.H. Hall, Acta Metal. 1 (1953) 22–31.

[41] R.R. Prabhu, M. Abdul Khadar, Bull. Mater. Sci. 31 (2008) 511–515.

[42] F. Gu, S.F. Wang, M.K. Lü, G.J. Zhou, D. Xu, D.R. Yuan, J. Phys. Chem. B 108 (24) (2004) 8119–8123.

[43] V. Senthilkumar, P. Vickraman, M. Jayachandran, C. Sanjeeviraja, J. Mater. Sci.: Mater. Electron. 21 (2010) 343–348.

[44] Q. Jiang, L.H. Liang, D.S. Zhao, J. Phys. Chem. B 105 (27) (2001) 6275–6277.

[45] N. Martin, C. Rousselot, D. Rondot, F. Palmino, R. Mercier, Thin Solid Films 300 (1997) 113–121.

[46] J. Pal, P. Chauhan, Mater. Charact. 61 (2010) 575–579.

[47] L. Wu, J.C. Yu, X. Wang, L. Zhang, J. Yu, J. Solid State Chem. 178 (2005) 321–328.

[48] A.M. Salem, M. Soliman Selim, J. Phys. D: Appl. Phys. 34 (2001) 12–17.

[49] R. Alexandrescu, F. Dumitrache, I. Morjan, I. Sandu, M. Savoiu, I. Voicu, C. Fleaca, R. Piticescu, Nanotechnology 15 (2004) 537–545.

[50] M. Radecka, K.Z. Akrzewska, H. Czternastek, T. Stapinski, S. Debrus, Appl. Surf. Sci. 65–66 (1993) 227–234.

[51] M.E. Aumer, S.F. LeBoeuf, S.M. Bedair, M. Smith, J.Y. Lin, H.X. Jiang, Appl. Phys. Lett. 77 (6) (2000).

[52] N. Daude, C. Gout, C. Jouanin, Phys. Rev. B 15 (1977) 3229–3235.

[53] N.D. Abazovic, M.I. Comor, M.D. Dramicanin, D.J. Jovanovic, S. Phillip Ahrenkiel, J.M. Nedeljkovic, J. Phys. Chem. B 110 (2006) 25366–25370.

[54] S.H. Luo, J.Y. Fan, W.L. Liu, M. Zhang, Z.T. Song, C.L. Lin, et al., Nanotechnology 17 (2006) 1695.

[55] R.W. Smith, A. Rose, Phys. Rev. 97 (1955) 1531–1537.

[56] S. Devi, S.G. Prakash, Natl. Acad. Sci. Lett. (India) 13 (1990) 35.

[57] R.K. Srivastava, S.G. Prakash, Natl. Acad. Sci. Lett. 30 (2007) 11–12.

[58] R.H. Bube, Photoconductivity of Solids, John Wiley and Sons, Inc., New York, 1967, p. 93.

[59] B. Borshchevskii, J. Phys. Chem. USSR 21 (1947) 1007.

[60] F. Stockmann, Z. Phys. 143 (1955) 348.

[61] J. Nelson, A.M. Eppler, I.M. Ballard, J. Photochem. Photobiol. A 148 (2002) 25–31.

[62] J.F. Randall, J.H.F. Wilkins, Proc. Roy. Soc. A 184 (1945) 366–389.

[63] R.H. Bube, Photoconductivity of Solids, John Wiley, New York, 1967.

[64] N. Pal, M. Paul, A. Bera, D. Basak, A. Bhaumik, Anal. Chim. Acta 674 (2010) 96–101.

[65] G. Boschloo, A. Hagfeldt, J. Phys. Chem. B 109 (24) (2005) 12093–12098.

[66] N. Kopidakis, K.D. Benkstein, J. van de Lagemaat, A.J. Frank, Q. Yuan, E.A. Schiff, Phys. Rev. B 73 (2006) 045326.

[67] A. Gupta, N.K. Verma, H.S. Bhatti, Appl. Phys. B 87 (2007) 311–315.

[68] A. Singh, J. Hanisch, V. Matias, F. Ronning, N. Mara, D. Pohl, B. Rellinghaus, D. Reagor, Nanotechnology 21 (2010) 415303, 5pp.

[69] A.C. Papageorgiou, N.S. Beglitis, C.L. Pang, G. Teobaldi, G. Cabailh, Q. Chen, et al., PNAS 107 (6) (2010) 2391–2396.

[70] R.H. Bube, Photoconductivity of Solids, John Wiley and Sons, Inc., New York, 1967, pp. 318–319.

[71] R.H. Bube, Photoconductivity of Solids, John Wiley and Sons, Inc., New York, 1967, p. 60.

[72] K. Sarmah, R. Sarma, Bull. Mater. Sci. 32 (2009) 369–373.

[73] R. Janes, M. Edge, J. Robinson, J. Rigby, N. Allen, J. Photochem. Photobiol. A: Chem. 127 (1999) 111–115.

[74] H.K. Yadav, K. Sreenivas, V. Gupta, Appl. Phys. Lett. 96 (2010) 223507.